Investigation of post-glaucoma-surgery structures by three-dimensional and polarization sensitive anterior eye segment optical coherence tomography◊

Yoshiaki Yasuno[1,4], Masahiro Yamanari[1,4], Keisuke Kawana[2,4], Tetsuro Oshika[2,4], and Masahiro Miura[3,4]

[1] *Computational Optics Group in the University of Tsukuba, Tsukuba, Ibaraki, Japan*
[2] *Department of Ophthalmology, University of Tsukuba, Tsukuba, Ibaraki, Japan*
[3] *Department of Ophthalmology, Tokyo Medical University, Shinjuku, Tokyo, Japan*
[4] *Computational Optics and Ophthalmology Group*

yasuno@optlab2.bk.tsukuba.ac.jp

http://optics.bk.tsukuba.ac.jp/COG/

Abstract: A sequential case series of post-glaucoma-surgery structures examined by three-dimensional corneal and anterior eye segment optical coherence tomography (3D-CASOCT) and 3D polarization sensitive CASOCT (PS-CASOCT) is presented. A total of 5 patients who underwent glaucoma surgery were included in this study. Of these, 1, 1, and 3 patient underwent trabeculotomy, laser iridotomy, and trabeculectomy respectively. One patient each who had undergone trabeculotomy or laser iridotomy was examined using a prototype 3D-CASOCT. This prototype is based on swept-source OCT technology, uses a probe beam with a center wavelength of 1.31 μm, and has an axial resolution of 11.6 μm and a scanning speed of 20,000 A lines/s. All 3 patients who underwent trabeculectomy were examined by PS-CASOCT, which has similar specifications to those of 3D-CASOCT, measures the depth-resolved birefringence of a specimen, and yields conventional OCT images. Detailed 3D visualization of the incision site of trabeculotomy and the ablation site of laser iridotomy was achieved using 3D-CASOCT. PS-CASOCT revealed, in addition to the structural details, the birefringent properties of the tissues of the trabeculectomy bleb. Some blebs showed abnormal birefringence in the conjunctiva and in a remnant fluid pool. This may indicate the existence of fibrosis in these regions. Both 3D-CASOCT and PS-CASOCT provide clinically significant information for the postoperative assessment of structures created during glaucoma surgery. Interactive 3D datasets of all cases are provided for interactive clinical review. Complex raw 3D OCT volumes are also provided as a reference dataset for the development of PS-OCT algorithms.

OCIS codes: (170.4500) Optical coherence tomography; (170.4470) Ophthalmology; (170.4460) Ophthalmic optics and devices; (170.1610) Clinical applications; (170.3880) Medical and biological imaging; (170.2655) Functional monitoring and imaging; (170.6935) Tissue characterization; (170.1020) Ablation of tissue

◊**Datasets associated with this article are available at** http://hdl.handle.net/10376/1238.

#99788 - $15.00 USD Received 5 Aug 2008; revised 22 Jan 2009; accepted 25 Jan 2009; published 2 Mar 2009

References and links

1. B. Thylefors and A. D. Négrel, "The global impact of glaucoma," Bull World Health Organ. **72**, 323–326 (1994).
2. B. Thylefors, A. D. Ngrel, R. Pararajasegaram, and K. Y. Dadzie, "Global data on blindness," Bull World Health Organ. **73**), 115–121 (1995).
3. C. F. Burgoyne, J. C. Downs, A. J. Bellezza, J.-K. F. Suh, and R. T. Hart, "The optic nerve head as a biomechanical structure: a new paradigm for understanding the role of IOP-related stress and strain in the pathophysiology of glaucomatous optic nerve head damage," Prog. Retin. Eye Res. **24**, 39–73 (2005).
4. D. Huang, E. A. Swanson, C. P. Lin, W. G. S. J. S. Schuman, W. Chang, T. F. M. R. Hee, K. Gregory, C. A. Puliafito, and J. G. Fujimoto, "Optical coherence tomography," Science **254**, 1178–1181 (1991).
5. E. A. Swanson, J. A. Izatt, M. R. Hee, D. Huang, C. P. Lin, J. S. Schuman, C. A. Puliafito, and J. G. Fujimoto, "In-vivo retinal imaging by optical coherence tomography," Opt. Lett. **18**, 1864–1866 (1993).
6. J. A. Izatt, M. R. Hee, E. A. Swanson, C. P. Lin, D. Huang, J. S. Schuman, C. A. Puliafito, and J. G. Fujimoto, "Micrometer-scale resolution imaging of the anterior eye in vivo with optical coherence tomography," Arch. Ophthalmol. **112**, 1584–1589 (1994).
7. S. Radhakrishnan, A. Rollins, J. Roth, S. Y. V. Westphal, D. Bardenstein, and J. Izatt, "Real-time optical coherence tomography of the anterior segment at 1310 nm," Arch. Ophthalmol. **119**, 1179–1185 (2001).
8. A. F. Fercher, C. K. Hitzenberger, G. Kamp, and S. Y. El-Zaiat, "Measurement of intraocular distances by backscattering spectral interferometry," Opt. Commun. **117**, 43–48 (1995).
9. G. Häusler and M. W. Lindner, ""Coherence rader" and "spectral radar" —New tools for dermatological diagnosis," J. Biomed. Opt. **3**, 21–31 (1998).
10. M. Wojtkowski, R. Leitgeb, A. Kowalczyk, T. Bajraszewski, and A. F. Fercher, "In vivo human retinal imaging by Fourier domain optical coherence tomography," J. Biomed. Opt. **7**, 457–463 (2002).
11. N. A. Nassif, B. Cense, B. H. Park, M. C. Pierce, S. H. Yun, B. E. Bouma, G. J. Tearney, T. C., Chen, and J. F. de Boer, "*In vivo* high-resolution video-rate spectral-domain optical coherence tomography of the human retina and optic nerve," Opt. Express **12**, 367–376 (2004) .
12. S. Yun, G. Tearney, B. Bouma, B. Park, and J. de Boer, "High-speed spectral-domain optical coherence tomography at 1.3 μm wavelength," Opt. Express **11**, 3598–3604 (2003).
13. Y. Yasuno, V. D. Madjarova, S. Makita, M. Akiba, A. Morosawa, C. Chong, T. Sakai, K. Chan, M. Itoh, and T. Yatagai, "Three-dimensional and high-speed swept-source optical coherence tomography for in vivo investigation of human anterior eye segments," Opt. Express **13**, 10652–10664 (2005).
14. K. Kawana, Y. Yasuno, T. Yatagai, and T. Oshika, "High-Speed, swept-source optical coherence tomography: a 3-dimensional view of anterior chamber angle recession," Acta Ophthalmol. Scand. **85**(6), 684–685 (2007).
15. M. Miura, H. Mori, Y. Watanabe, M. Usui, K. Kawana, T. Oshika, T. Yatagai, and Y. Yasuno, "Three-dimensional optical coherence tomography of granular corneal dystrophy," Cornea **26**, 373–374 (2007).
16. M. Miura, K. Kawana, T. Iwasaki, T. Kikuchi, T. Oshika, H. Mori, M. Yamanari, S. Makita, T. Yatagai, and Y. Yasuno, "Three-dimensional Anterior Segment Optical Coherence Tomography of Filtering Blebs After Trabeculectomy," J. Glaucoma **17**, 193–196 (2008).
17. C. Kerbage, H. Lim, W. Sun, M. Mujat, and J. F. de Boer, "Large depth-high resolution full 3D imaging of the anterior segments of the eye using high speed optical frequency domain imaging," Opt. Express **15**, 7117–7125 (2007).
18. M. V. Sarunic, S. Asrani, and J. A. Izatt, "Imaging the Ocular Anterior Segment With Real-Time, Full-Range Fourier-Domain Optical Coherence Tomography," Arch. Ophthalmol. **126**, 537–542 (2008).
19. S. Asrani, M. Sarunic, C. Santiago, and J. Izatt, "Detailed Visualization of the Anterior Segment Using Fourier-Domain Optical Coherence Tomography," Arch. Ophthalmol. **126**, 765–771 (2008).
20. M. R. Chalita, Y. Li, S. Smith, C. Patil, V. Westphal, A. M. Rollins, J. A. Izatt, and D. Huang, "High-speed optical coherence tomography of laser iridotomy," Am. J. Ophthalmol. **140**, 1133–1136 (2005).
21. X. J. Wang, T. E. Milner, and J. S. Nelson, "Characterization of fluid flow velocity by optical Doppler tomography," Opt. Lett. **20**, 1337–1339 (1995).
22. Z. Chen, T. E. Milner, D. Dave, and J. S. Nelson, "Optical Doppler tomographic imaging of fluid flow velocity in highly scattering media," Opt. Lett. **22**, 64–66 (1997).
23. B. R. White, M. C. Pierce, N. Nassif, B. Cense, B. H. Park, G. J. Tearney, B. E. Bouma, T. C. Chen, and J. F. de Boer, "*In vivo* dynamic human retinal blood flow imaging using ultra-high-speed spectral domain optical coherence tomography," Opt. Express **11**, 3490–3497 (2003).
24. R. A. Leitgeb, L. Schmetterer, W. Drexler, A. F. Fercher, R. J. Zawadzki, and T. Bajraszewski, "Real-time assessment of retinal blood flow with ultrafast acquisition by color Doppler Fourier domain optical coherence tomography," Opt. Express **11**, 3116–3121 (2003).
25. S. Makita, Y. Hong, M. Yamanari, T. Yatagai, and Y. Yasuno, "Optical coherence angiography," Opt. Express **14**, 7821–7840 (2006).
26. K. D. Rao, M. A. Choma, S. Yazdanfar, A. M. Rollins, and J. A. Izatt, "Molecular contrast in optical coherence tomography by use of a pump probe technique," Opt. Lett. **28**, 340–342 (2003).

#99788 - $15.00 USD Received 5 Aug 2008; revised 22 Jan 2009; accepted 25 Jan 2009; published 2 Mar 2009

27. B. E. Applegate, C. Yang, and J. A. Izatt, "Theoretical comparison of the sensitivity of molecular contrast optical coherence tomography techniques," Opt. Express **13**, 8146–8163 (2005).
28. Y. Hori, Y. Yasuno, S. Sakai, M. Matsumoto, T. Sugawara, V. Madjarova, M. Yamanari, S. Makita, T. Yasui, T. Araki, M. Itoh, and T. Yatagai, "Automatic characterization and segmentation of human skin using three-dimensional optical coherence tomography," Opt. Express **14**, 1862–1877 (2006).
29. Y. Hong, S. Makita, M. Yamanari, M. Miura, S. Kim, T. Yatagai, and Y. Yasuno, "Three-dimensional visualization of choroidal vessels by using standard and ultra-high resolution scattering optical coherence angiography," Opt. Express **15**, 7538–7550 (2007).
30. Y. Yasuno, Y. Hong, S. Makita, M. Yamanari, M. Akiba, M. Miura, and T. Yatagai, "In vivo high-contrast imaging of deep posterior eye by 1-um swept source optical coherence tomography and scattering optical coherence angiography," Opt. Express **15**, 6121–6139 (2007).
31. C. A. Lingley-Papadopoulos, M. H. Loew, M. J. Manyak, and J. M. Zara, "Computer recognition of cancer in the urinary bladder using optical coherence tomography and texture analysis," J. Biomed. Opt. **13**, 024003 (pages 9) (2008).
32. C. Xu, J. M. Schmitt, S. G. Carlier, and R. Virmani, "Characterization of atherosclerosis plaques by measuring both backscattering and attenuation coefficients in optical coherence tomography," J. Biomed. Opt. **13**, 034003 (pages 8) (2008).
33. J. F. de Boer, T. E. Milner, M. J. C. van Gemert, and J. S. Nelson, "Two-dimensional birefringence imaging in biological tissue by polarization-sensitive optical coherence tomography," Opt. Lett. **22**, 934–936 (1997).
34. J. F. de Boer, T. E. Milner, and J. S. Nelson, "Determination of the depth-resolved Stokes parameters of light backscattered from turbid media by use of polarization-sensitive optical coherence tomography," Opt. Lett. **24**, 300–302 (1999).
35. S. Jiao and L. V. Wang, "Two-dimensional depth-resolved Mueller matrix of biological tissue measured with double-beam polarization-sensitive optical coherence tomography," Opt. Lett. **27**, 101–103 (2002).
36. S. Jiao, M. Todorović, G. Stoica, and L. V. Wang, "Fiber-based polarization-sensitive Mueller matrix optical coherence tomography with continuous source polarization modulation," Appl. Opt. **44**, 5463–5467 (2005).
37. Y. Yasuno, S. Makita, Y. Sutoh, M. Itoh, and T. Yatagai, "Birefringence imaging of human skin by polarization-sensitive spectral interferometric optical coherence tomography," Opt. Lett. **27**, 1803–1805 (2002).
38. Y. Yasuno, S. Makita, T. Endo, M. Itoh, T. Yatagai, M. Takahashi, C. Katada, and M. Mutoh, "Polarization-sensitive complex Fourier domain optical coherence tomography for Jones matrix imaging of biological samples," Appl. Phys. Lett. **85**, 3023–3025 (2004).
39. E. Götzinger, M. Pircher, and C. K. Hitzenberger, "High speed spectral domain polarization sensitive optical coherence tomography of the human retina," Opt. Express. **12**, 10,217–10,229 (2005).
40. S. Makita, Y. Yasuno, T. Endo, M. Itoh, and T. Yatagai, "Polarization contrast imaging of biological tissues by polarization-sensitive Fourier-domain optical coherence tomography," Appl. Opt. **45**, 1142–1147 (2006).
41. M. Yamanari, S. Makita, V. D. Madjarova, T. Yatagai, and Y. Yasuno, "Fiber-Based Polarization-Sensitive Fourier Domain Optical Coherence Tomography using B-Scan-Oriented Polarization Modulation Method," Opt. Express **14**, 6502–6515 (2006).
42. B. Cense, M. Mujat, T. C. Chen, B. H. Park, and J. F. de Boer, "Polarization-sensitive spectral-domain optical coherence tomography using a single line scan camera," Opt. Express **15**, 2421–2431 (2007).
43. W. Oh, S. Yun, B. Vakoc, M. Shishkov, A. Desjardins, B. Park, J. de Boer, G. Tearney, and B. Bouma, "High-speed polarization sensitive optical frequency domain imaging with frequency multiplexing," Opt. Express **16**, 1096–1103 (2008).
44. W. Y. Oh, B. J. Vakoc, S. H. Yun, G. J. Tearney, and B. E. Bouma, "Single-detector polarization-sensitive optical frequency domain imaging using high-speed intra A-line polarization modulation," Opt. Lett. **33**, 1330–1332 (2008).
45. B. Cense, T. C. Chen, B. H. Park, M. C. Pierce, and J. F. de Boer, "In vivo depth-resolved birefringence measurements of the human retinal nerve fiber layer by polarization-sensitive optical coherence tomography," Opt. Lett. **27**, 1610–1612 (2002).
46. M. Yamanari, M. Miura, S. Makita, T. Yatagai, and Y. Yasuno, "Phase retardation measurement of retinal nerve fiber layer by polarization-sensitive spectral-domain optical coherence tomography and scanning laser polarimetry," J. Biomed. Opt. **13**, 014013 (pages 10) (2008).
47. M. Pircher, E. Götzinger, O. Findl, S. Michels, W. Geitzenauer, C. Leydolt, U. Schmidt-Erfurth, and C. K. Hitzenberger, "Human macula investigated in vivo with polarization-sensitive optical coherence tomography," Inv. Ophthalmol. Vis. Sci. **47**, 5487–5494 (2006).
48. M. Miura, M. Yamanari, T. Iwasaki, A. E. Elsner, S. Makita, T. Yatagai, and Y. Yasuno, "Imaging Polarimetry in Age-Related Macular Degeneration," Invest. Ophthalmol. Vis. Sci. **49**, 2661–2667 (2008).
49. M. Pircher, E. Götzinger, R. Leitgeb, and C. K. Hitzenberger, "Transversal phase resolved polarization sensitive optical coherence tomography," Phys. Med. Biol. **49**, 1257–1263 (2004).
50. C. K. Hitzenberger, E. Götzinger, and M. Pircher, "Birefringence properties of the human cornea measured with polarization sensitive optical coherence tomography." Bull Soc Belge Ophtalmol. (302), 153–168 (2006).
51. E. Götzinger, M. Pircher, I. Dejaco-Ruhswurm, S. Kaminski, C. Skorpik, and C. K. Hitzenberger, "Imaging of

#99788 - $15.00 USD Received 5 Aug 2008; revised 22 Jan 2009; accepted 25 Jan 2009; published 2 Mar 2009

birefringent properties of keratoconus corneas by polarization-sensitive optical coherence tomography." Invest. Ophthalmol. Vis. Sci. **48**, 3551–3558 (2007).
52. M. Yamanari, S. Makita, and Y. Yasuno, "Polarization-sensitive swept-source optical coherence tomography with continuous source polarization modulation," Opt. Express **16**, 5892–5906 (2008).
53. C. Chong, A. Morosawa, and T. Sakai, "High-speed wavelength-swept laser source with high-linearity sweep for optical coherence tomography," IEEE J. Sel. Top. Quantum Electron. **14**, 235–242 (2008).
54. R. A. Leitgeb, C. K. Hitzenberger, and A. F. Fercher, "Performance of fourier domain vs. time domain optical coherence tomography," Opt. Express **11**, 889–894 (2003).
55. K. Kawana, T. Kiuchi, Y. Yasuno, and T. Oshika, "Evaluation of trabeculectomy blebs by using three-dimensional cornea and anterior segment optical coherence tomography," Ophthalmology, accepted to publication.
56. I. P. Pollack, "Current concepts in laser iridotomy," Int. Ophthalmol. Clin. **24**, 153–180 (1984).
57. A. L. Schwartz, N. F. Martin, and P. A. Weber, "Corneal decompensation after argon laser iridectomy," Arch. Ophthalmol. **106**, 1572–1574 (1988).
58. Y. Yamamoto, T. Uno, K. Shisida, L. Xue, A. Shiraishi, X. Zheng, and Y. Ohashi, "Demonstration of aqueous streaming through a laser iridotomy window against the corneal endothelium," Arch. Ophthalmol. **124**, 387–393 (2006).

1. Introduction

Glaucoma is one of the major causes of blindness; it affects up to 22.5 million people in the world and is responsible for 5.2 million cases of blindness [1, 2]. Although the detailed mechanism underlying this disease remains unclear, elevation of intraocular pressure (IOP) is known to play an etiologic role in glaucoma. One of the possible mechanisms of glaucoma development is as follows. Elevated IOP triggers the disease and applies mechanical stress to the biomechanical structures of the optic nerve head (ONH) [3] and/or disturbs ocular circulation. The disorder induced by the mechanical stress and the dysfunction of ocular circulation trigger optic neuropathy.

The only effective strategy for the suppression of glaucoma progression is the reduction of IOP. While pharmacological interventions to reduce IOP are effective in the early stage, surgical intervention, including trabeculectomy, trabeculotomy, and laser iridotomy, are required in advanced or some specific cases. In these surgeries, artificial tissue structures that bypass the drainage of the aqueous humor are created. It is crucial to investigate the morphology of these artificial tissue structures in order to assess their function. The structures include a filtering bleb of trabeculectomy, ablated trabecular meshwork of trabeculectomy, and an abrated hole on the iris of laser iridotomy.

A slit-lamp microscope and an ultrasound biomicroscope (UBM) can be used to observe these structures. However, the slit-lamp microscope cannot reveal the internal morphology of the artificial tissue structure. The UBM on the other hand can reveal the internal structure, but the obtained images are two-dimensional (2D). Furthermore, UBM examination carries a risk of infection since contact with the eye is required. Corneal and anterior segment optical coherence tomography (CAS-OCT) is an emerging modality that can overcome these limitations.

OCT is a noninvasive optical modality that provides cross-sectional images of *in vivo* tissue at a resolution in the micrometer scale [4]. In the field of ophthalmology, OCT was first applied for retinal imaging [5] and subsequently for the examination of the anterior eye [6, 7]. OCT remained a 2D modality until the development of Fourier domain OCT (FD-OCT) techniques, including spectral-domain OCT (SD-OCT) [8–11] and swept-source OCT (SS-OCT) [12]. This high-speed alternative to conventional OCT (time-domain OCT; TD-OCT) has accelerated the acquisition speed of OCT and enabled the three-dimensional (3D) in vivo examination of human eyes. The first *in vivo* high-speed 3D anterior segment OCT was performed by the authors in 2005 [13] and was used in several clinical case studies [14–16]. Currently, several groups are working to develop different methods for the 3D examination of the anterior eye, and promising results have been presented [17–19].

Although 2D and 3D CAS-OCT can be used for the structural assessment of the eye af-

#99788 - $15.00 USD Received 5 Aug 2008; revised 22 Jan 2009; accepted 25 Jan 2009; published 2 Mar 2009

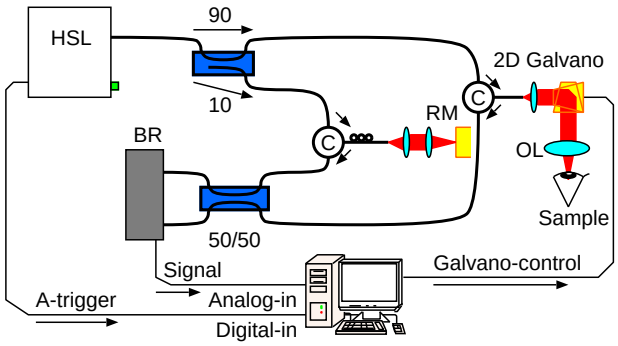

Fig. 1. Optical scheme of 3D-CASOCT. HSL: high-speed wavelength-scanning light source, C: circulator, RM: reference mirror, OL: objective, and BR: balanced photoreceiver.

ter glaucoma surgery [16, 20, 55], they do not provide significant information about the tissue property at the surgical site. This is because OCT is only sensitive to backscattering light intensity and not to the other optical properties of tissues. Functional extensions of OCT, such as Doppler OCT [21–25] and molecular-contrast OCT [26, 27], as well as post-processing algorithms [28–32] have been studied in order to develop a new type of OCT that can detect multiple optical properties. Polarization -sensitive OCT (PS-OCT) [33–36], including its Fourier domain version [37–44], has emerged as one of the most promising modalities. PS-OCT provides not only conventional OCT intensity images (*I*-OCT images) but also a full set or a subset of polarization-sensitive tomographies, including phase-retardation OCT, axis orientation tomography, and diattenuation tomography. When used for the examination of the posterior eye, this modality demonstrates superior performance with regard to assessment of the retinal nerve fiber layer [45, 46] and investigation for age-related macular degeneration [47, 48]. However, only a few studies have focused on the application of PS-OCT to the anterior eye [49–52].

This paper aims at providing a reference case series in which tissue structures created during glaucoma surgery were postoperatively examined using non-polarization-sensitive high-speed 3D CAS-OCT (3D-CASOCT) [13] and its polarization-sensitive extension (3D polarization-sensitive CAS-OCT; PS-CASOCT) [52]. One patient each who had undergone trabeculotomy or laser iridotomy was examined using 3D-CASOCT. The filtering blebs in the 3 patients who underwent trabeculectomy were measured using PS-CASOCT.

2. Methods

2.1. Three-Dimensional Corneal and Anterior Eye Segment OCT

The postoperative structure of the surgical sites were examined using 3D-CASOCT. Figure 1 shows a schematic of our 3D-CASOCT system. It is based on a standard SS-OCT system. The light source (HSL-2000; Santec, Japan) [53] has a center wavelength of 1.31μm, a scanning bandwidth of 110 nm, a scanning speed of 20 KHz, a lasing duty exceeding 50%, and 3-dB single-path coherence length of 6mm. This spectral property and scanning speed provide a depth resolution of 11.6 μm in air and a measurement speed of 20,000 A lines/s. The light from the light source passes through a fiber Mach-Zehnder interferometer and then illuminates the anterior eye of the patient. A 2D galvanometric scanner scans the probe light according to a raster-scanning protocol. The backscattered probe beam and the reference beam produce spectral interference signals on a balanced photodetector. The interference signal is digitized and is sampled at a sampling frequency of 60 MHz with a digitization resolution of 14 bits. A

#99788 - $15.00 USD Received 5 Aug 2008; revised 22 Jan 2009; accepted 25 Jan 2009; published 2 Mar 2009

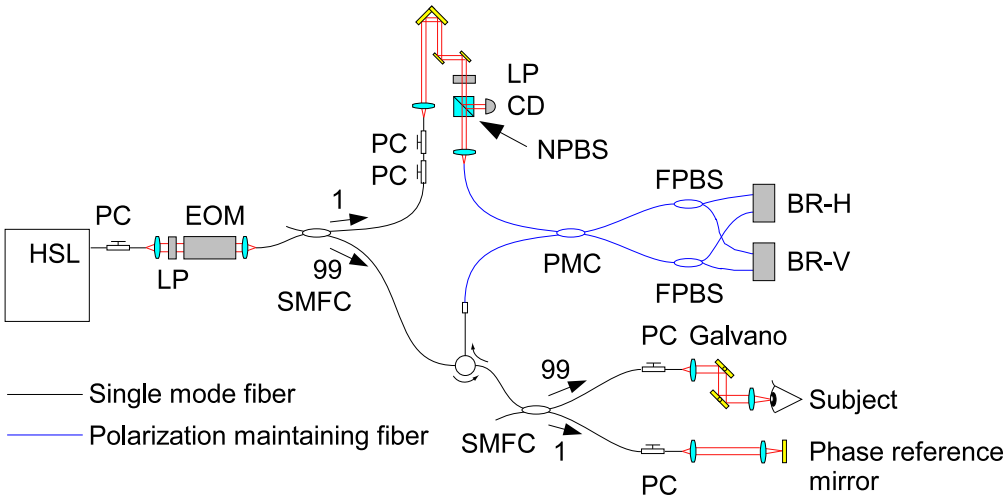

Fig. 2. Optical scheme of 3D PS-CASOCT. HSL: high-speed wavelength-scanning light source, PC: fiber polarization controller, LP: linear polarizer, EOM: electro-optic polarization modulator, SMFC: single-mode fiber coupler, CD: a calibration detector used in the system-building and alignment process, PMC: polarization-maintaining fiber coupler, FPBS: fiber polarization beam splitter, and BR-H and BR-V: balanced photoreceivers for the horizontal and vertical polarization-detection channels respectively.

standard image-reconstruction algorithm for SS-OCT is applied to the digitized spectra, and a 3D tomographic image of the anterior eye is obtained.

A typical 3D OCT volume contains 200 $\times$ 200 A-lines, and its acquisition time is 2 s. The typical optical power of the cornea is 5 mW, and sensitivity is 107 dB. The details of this 3D-CASOCT are described in ref. [13].

2.2. Polarization Sensitive Corneal and Anterior Eye Segment OCT

Figure 2 shows an optical schematic of the PS-CASOCT used in this study. This schematic is similar to that presented in section 2.1, except for the following 3 significant differences.

The first difference is in the phase-stabilization mechanism. A portion of the probe beam (1%) was trapped and used to illuminate a phase reference mirror. The OCT signal reflected by this reference mirror produces a reference phase, and inter A-line fluctuation of OCT phase is canceled by using this reference phase. This phase stabilization process is mandatory to remove fixed pattern noises originated from the multiple reflections mainly from an electro-optic polarization modulator (EOM) in a source arm and polarization maintaining fiber components in a detection arm of the interferometer. After this phase stabilization, the fixed pattern noises is canceled by a standard average-subtraction algorithm, in which the average of the spectra in an entire B-scan is subtracted from the each individual signal spectrum of the B-scan.

The second difference is the introduction of the EOM in the source arm. The EOM sinusoidally modulates the phase of a single polarization component of the source light, while the orthogonal polarization component is not modulated. The reference arm was configured to sinusoidally modulate the phase of the reference beam in both polarization components. Hence, 2 polarization components are multiplexed in a single spectral interference signal, in which the first polarization component is not altered, while the intensity of the second is modulated.

The third difference is the presence of a polarization-sensitive scheme in the detection arm. The polarization-sensitive detector pair simultaneously acquires 2 spectral interference

#99788 - $15.00 USD Received 5 Aug 2008; revised 22 Jan 2009; accepted 25 Jan 2009; published 2 Mar 2009

signals whose polarizations are orthogonal to each other. Since the polarization axis of this polarization-sensitive detector pair is not identical to that of the polarization modulation, each single spectral interference signal contains 2 multiplexed polarization components. The multiplexed polarization components are de-multiplexed by using numerical Fourier transform technique, and finally, 4 polarization-sensitive spectra are obtained.

The 4 OCT signals obtained from this spectral set are fed into a Jones matrix-based PS-OCT algorithm [41, 52], and a set of PS-OCT images are obtained, which included cumulative phase-retardation OCT (φ-OCT), axis-orientation OCT, and diattenuation OCT images.

A polarization-diversity intensity-OCT (*PD*-OCT) image, which has similar properties to those of conventional OCT images, was created by averaging the intensities of the 2 OCT images obtained using 2 non-modulated polarization components acquired via 2 detection channels.

Real-time conventional intensity OCT images are reconstructed and displayed during a clinical measurement session, while the polarization sensitive OCT images are reconstructed after closing the measurement session.

It should be noted that the phase-retardation value measured by PS-CASOCT is wrapped and folded within the range of 0 to π radians in the following manner:

$$\phi' = \begin{cases} \phi & : 0 \leq \phi < \pi \\ 2\pi - \phi & : \pi \leq \phi < 2\pi \end{cases} \quad (1)$$

where ϕ is the true cumulative phase retardation of the sample, and ϕ' is the phase-retardation value obtained using our PS-CASOCT system.

The depth resolution and sensitivity were 11.9 μm in air and 102 dB at 570 μm from the zero-delay point respectively. The power on the cornea was 2.0 mW. Further details regarding this PS-CASOCT can be found in ref. [52].

3. Case Series

3.1. Subjects

This study included 4 glaucoma patients and 1 patient with primary angle closure. Of the 5 patients, 1, 1, and 3 patient underwent trabeculotomy, laser iridotomy, and trabeculectomy respectively. The details of the subjects are summarized in Table 1.

The examination protocol was designed to adhere to the tenets of the Declaration of Helsinki and was approved by the institutional review boards of the University of Tsukuba and Tokyo Medical University. Written informed consent was obtained prior to 3D-CASOCT and PS-CASOCT imaging.

In this case series, the scanning protocols of OCT depended on the individual subjects. The details of the scanning protocol are summarized in Table 2. The number of A-lines in this table is not necessarily equal to originally obtained OCT volume, because of the truncation of the area-of-interest. Although the volumetric measurements took a few seconds, the fixation of the eyes of the subjects were sufficiently stable, hence no method to cancel the eye motion was applied.

3.2. Case 1: 3D-CASOCT of Trabeculotomy

The patient was a 53-year-old Asian woman with a history of secondary steroid induced glaucoma (SIG). The IOP of the right eye was 45 mm Hg. Trabeculotomy was performed in her right eye in Tsukuba University Hospital, and the postoperative IOP was reduced to 13 mm Hg. Measurement with 3D-CASOCT was performed 45 days after the surgery by using a raster-scanning protocol with 200 $\times$ 200 A-lines.

#99788 - $15.00 USD Received 5 Aug 2008; revised 22 Jan 2009; accepted 25 Jan 2009; published 2 Mar 2009

Table 1. The list of the subjects involved in this study. L/R indicates which eye was involved (left or right), pre- and post-IOP indicate the pre- and postoperative IOP in mm Hg. SIG, PAC, NVG, and POAG are steroid-induced glaucoma, primary angle closure, neovascular glaucoma, and primary open angle glaucoma, respectively. †Age indicates the age of the patient at the time of surgery, except for subject 6, for whom it indicates the age on the day of OCT examination. ‡F stands for female and M for male.

ID	Disease	Surgical Type	Age†	Sex‡	L/R	Pre-IOP	Post-IOP
1	SIG	Trabeculotomy	53	F	R	45	13
2	PAC	Laser Iridotomy	59	F	L	14	9
3	NVG	Trabeculectomy	69	M	R	35	8
4	SIG	Trabeculectomy	66	F	R	44	18
5	POAG	Trabeculectomy	46	F	R	40	28
6	Normal	None	48	M	R	NA	NA

Table 2. Detailed parameters of scanning. The number (#) of voxels, volume size, and voxels size are represented as horizontal × vertical × depth. AQT is the acquisition time of OCT.

Case	System	# of Voxels	Volume size [mm^3]	Voxel size [μm^3]	AQT [s]
1	3D	190 × 200 × 660	9.8 × 10.3 × 5.1	51.5 × 51.5 × 7.7	2.0
2	3D	190 × 200 × 660	4.9 × 5.1 × 5.5	25.6 × 25.6 × 8.3	2.0
3	PS	512 × 140 × 525	5.0 × 5.0 × 4.1	9.8 × 35.7 × 7.8	3.8
4	PS	512 × 140 × 525	10.0 × 10.0 × 4.1	19.5 × 71.4 × 7.8	3.8
5	PS	512 × 140 × 525	10.0 × 10.0 × 4.1	19.5 × 71.4 × 7.8	3.8
6	PS	512 × 256 × 525	5.0 × 5.0 × 4.1	9.8 × 19.5 × 7.8	6.9

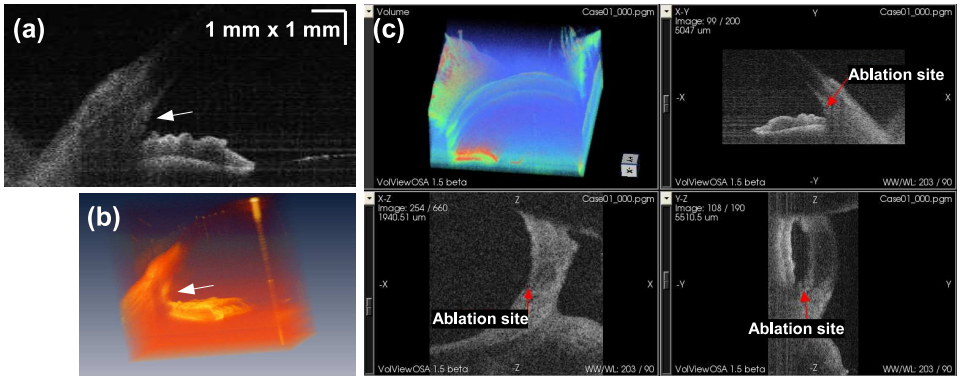

Fig. 3. Patient 1: Trabeculotomy site. (a) A horizontal cross section extracted from a 3D OCT volume, and (b) a volume rendering of the same OCT volume. The white arrows in the images show the incision site of trabeculotomy. (c) A screen shot of 3D observation by VolViewOSA (VVO). The incision site is indicated by red arrows in horizontal, vertical and en-face cross sections. See View 1.

#99788 - $15.00 USD Received 5 Aug 2008; revised 22 Jan 2009; accepted 25 Jan 2009; published 2 Mar 2009

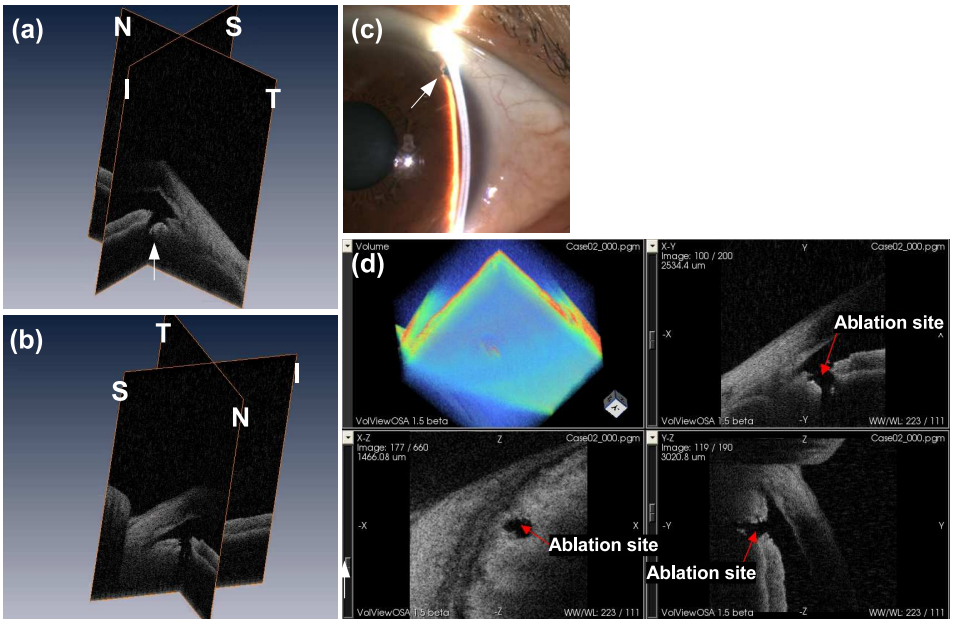

Fig. 4. Subject 2: Site of laser iridotomy. (a) and (b) show identical OCT volumes from different directions. T, S, N, and I indicate the temporal, superior, nasal, and inferior directions, respectively. The white arrows indicate the ablation hole (iridotomy channel) created by laser iridotomy. (c) An en-face photograph of the laser iridotomy site. The white arrow indicates the the iridotomy channel. (d) A screen shot of 3D observation by OSA ISP. The ablation site is indicated by red arrows in horizontal, vertical, and en-face cross sections. See View 2.

The incision site of trabeculotomy at the anterior chamber angle (see appendix C.1) was clearly visualized in the *I*-OCT image as show in in Figs. 3(a)-(c) (white arrows in Figs. 3(a) and (b)), and red arrows in Fig. 3(c)). The following properties of this trabeculotomy site were manually measured from this 3D dataset. The site was located 0.23 mm from the angle recess and the size of the ablated site was measured to be 0.17 mm $\times$ 0.08 mm. A full 3D dataset is available on-line for detailed observation (23.9 MB). See View 1.

3.3. Case 2: 3D-CASOCT of Laser Iridotomy

The patient was a 59-year-old Asian woman with a history of primary angle closure. During consultation at the Tsukuba University hospital, it was found that the anterior chambers of both eyes were shallow, and the IOP in both eyes was 14 mm Hg. Both eyes were classified as Shaffer grade 1, as determined by gonioscopic examination. Nd:YAG laser iridotomy was uneventfully performed in both eyes to prevent acute angle closure crisis. An ablation hole (see appendix C.2) of this patient was observed by a slit lamp examination as shown in Fig. 4(c).

One week after the surgery, the IOPs of the right and left eye were 8 and 9 mm Hg respectively. Her left eye was scanned by 3D-CASOCT. Figures 4(a) and (b) show the horizontal and vertical scans extracted from a single 3D *I*-OCT volume. Although the laser iridotomy site (white arrow) was very small, it could be easily targeted because of the 3D measurement capability of this CAS-OCT system. Perfect penetration of the iridotomy channel was clearly observed in this OCT volume. The full 3D dataset enables comprehensive observation of the ablation site as shown in Fig. 4(d). This 3D dataset is available on-line (23.9 MB). See View 2.

#99788 - $15.00 USD Received 5 Aug 2008; revised 22 Jan 2009; accepted 25 Jan 2009; published 2 Mar 2009

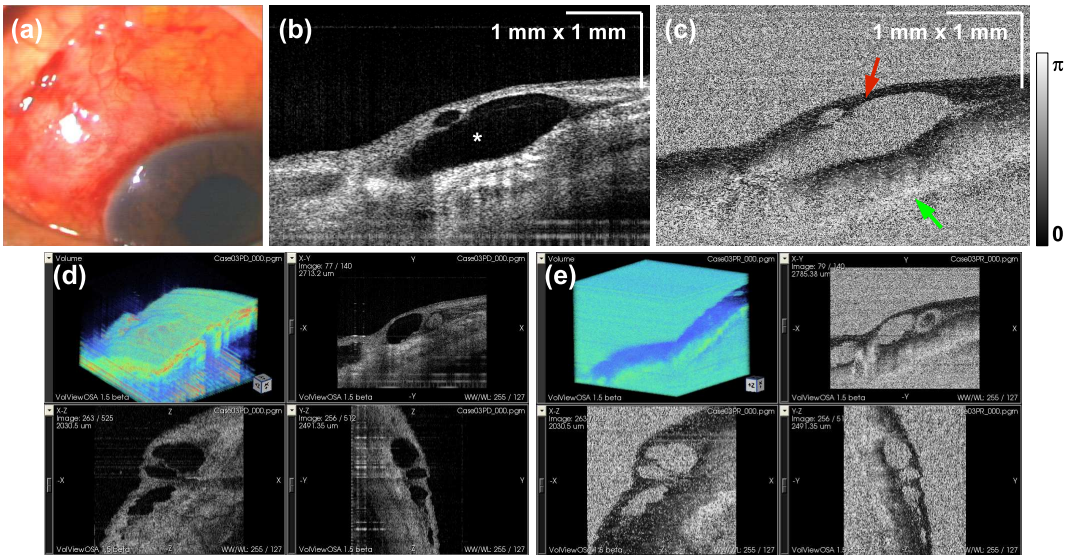

Fig. 5. Subject 3: (a) An en-face photograph of the filtering bleb. (b) A representative horizontal tomography of the filtering bleb extracted from a 3D *PD*-OCT volume acquired 1 week after the surgery. The asterisk (*) indicates a fluid pool. (c) A corresponding φ-OCT to that shown in (b) taken from a 3D φ-OCT volume. The green arrow indicates the strong birefringence of the sclera, and the red arrow indicates the non-birefringent appearance of the conjunctiva. (d), (e) Screen shots of 3D interactive observations of *PD*-OCT and φ-OCT by OSA ISP. See View 3 for *PD*-OCT and View 4 for φ-OCT.

The parameters associated with this laser iridotomy site were manually measured from this 3D OCT volume. The iridotomy hole measured 0.5 mm $\times$ 0.8 mm, and the volume removed by iridotomy was estimated to be 0.18 mm^3.

3.4. Case 3: PS-CASOCT of filtering bleb one week after trabeculectomy

The patient was a 69-year-old Asian man with a history of neovascular glaucoma with central vein occlusion in his right eye. He was referred for ophthalmic examination to Kasumigaura Hospital, Tokyo Medical University. He underwent trabeculectomy of the right eye because of increased IOP of 35 mm Hg despite pharmacological therapy. Four days after the surgery, a diffuse filtering bleb (see appendix C.3) was observed on slit-lamp examination (Fig. 5(a)), and the IOP was decreased to 8 mm Hg.

One week after the trabeculectomy, PS-CASOCT was performed on the filtering bleb. A *PD*-OCT revealed the internal structure of the filtering bleb as shown in Fig. 5(b). A fluid pool was clearly observed and is indicated by an asterisk (*) in Fig. 5(b). In the φ-OCT image shown in Fig. 5(c), marked birefringence was not observed in the conjunctiva, while strong birefringence was observed in the sclera. This contrasting appearance of birefringence is consistent with the finding in normal anterior eye segments.

The 3D interactive observation enables comprehensive and detailed observations of the *PD*-OCT and φ-OCT. These 3D datasets are available on-line. See View 3 for *PD*-OCT (35.9 MB) and View 4 for φ-OCT (35.9 MB).

A set of raw complex OCT volumes (1.0 GB) are also provided, which enables the readers to develop their own PS-OCT algorithm. For the details, see Appendix B.

#99788 - $15.00 USD Received 5 Aug 2008; revised 22 Jan 2009; accepted 25 Jan 2009; published 2 Mar 2009

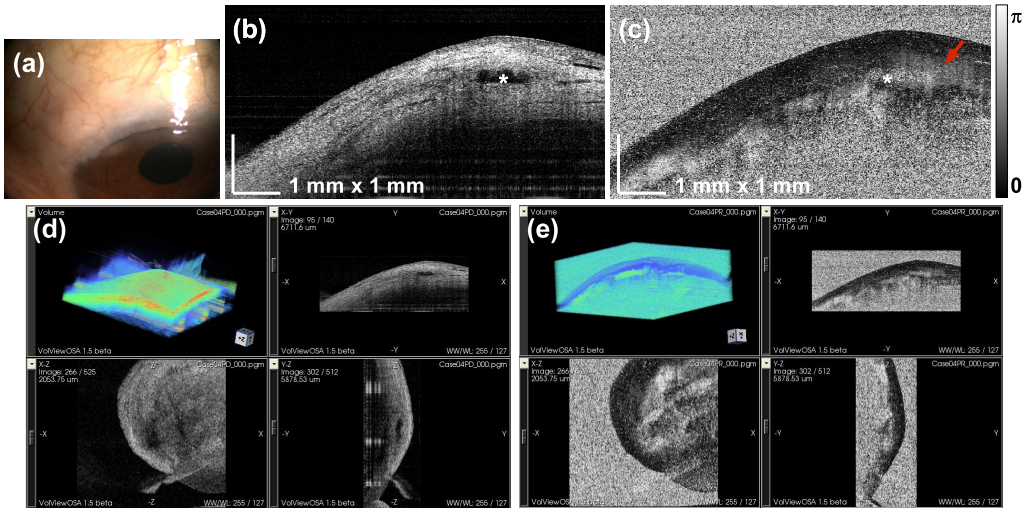

Fig. 6. Second examination of subject 4 2: (a) An en-face photograph of the filtering bleb. (b) A representative horizontal tomography of the filtering bleb extracted from a 3D *PD*-OCT volume taken 3 years after the surgery. The asterisk (*) indicates the fluid pool. (c) The corresponding φ-OCT. The red arrow indicates moderate birefringence around the anterior inner wall of the fluid pool. (d), (e) Screen shots of 3D interactive observations of *PD*-OCT and φ-OCT by OSA ISP. See View 5 for *PD*-OCT and View 6 for φ-OCT.

3.5. *Case 4: PS-CASOCT of filtering bleb three-year after trabeculectomy*

The patient was 66-year-old Asian woman, who originally suffered from adult-onset Still's disease, was medicated with steroids, and consequently developed steroid-induced glaucoma (SIG). She underwent fornix-based trabeculectomy in her right eye in Tsukuba University Hospital. During surgery, 0.04% mitomycin C was instilled into the eye, and a 4 mm $\times$ 4 mm scleral flap was created. The postoperative IOP was maintained at 18 mm Hg on treatment with topical latanoprost, while the preoperative IOP was 44 mm Hg.

A diffuse filtering bleb was observed at the 11 o'clock position on slit-lamp observation. Three year after the surgery, the filtering bleb was examined by non-polarization sensitive 3D-CASOCT. The detail of this 3D structural investigation was previously published (the second case of ref. [16]).

The same region was scanned by 3D PS-CASOCT 1 year after the first 3D-CASOCT examination (4 years after the surgery). The preceded slit-lamp examination did not reveal the internal structure of the bleb because of severe scarring of the conjunctiva (Fig. 6(a)). The *PD*-OCT image clearly depicted the fluid pool in the filtering bleb, as shown in Fig. 6(b) (white asterisk (*)). In the φ-OCT image shown in Fig. 6(c), moderate birefringence was observed around the anterior inner wall of the fluid pool. Since the normal conjunctiva is known not to exhibit birefringence, the observed birefringence may indicate fibrosis in this region, although further intensive studies are required for a more reliable conclusion.

The 3D interactive observation enables comprehensive and detailed observations of the *PD*-OCT and φ-OCT. These 3D datasets are available on-line. See View 5 for *PD*-OCT (35.9 MB) and View 6 for φ-OCT (35.9 MB).

A set of raw complex OCT volumes (1.0 GB) are also provided, which enables the readers to develop their own PS-OCT algorithm. For the details, see Appendix B.

#99788 - $15.00 USD Received 5 Aug 2008; revised 22 Jan 2009; accepted 25 Jan 2009; published 2 Mar 2009

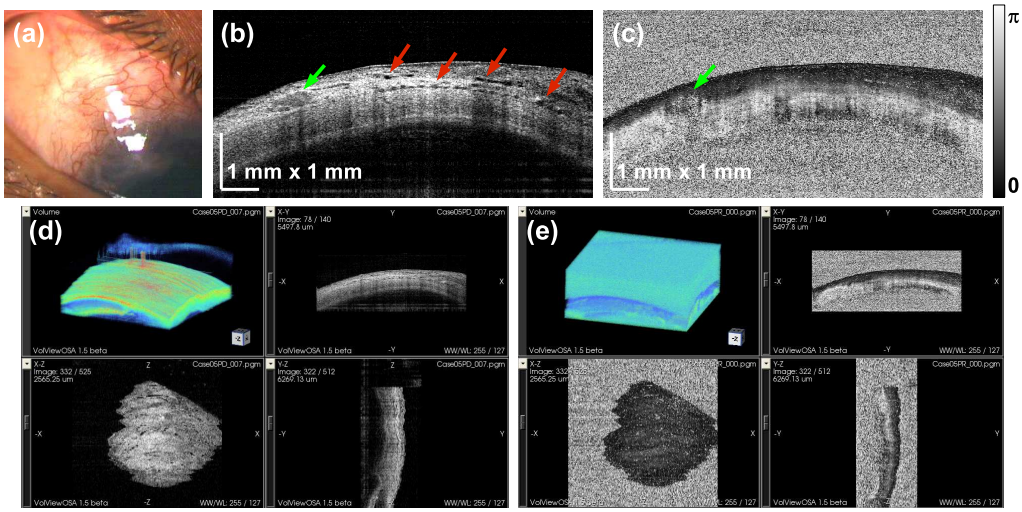

Fig. 7. Subject 5: (a) An en-face photograph of the filtering bleb. (b) A representative horizontal tomography of the filtering bleb extracted from a 3D *I*-OCT volume taken 4 years after the surgery. The red arrow indicates the remnant of the bleb. (c) The corresponding tomographic image taken from the corresponding φ-OCT volume. The green arrow indicates the position indicated by the green arrow in (b). (d), (e) Screen shots of 3D interactive observations of *PD*-OCT and φ-OCT by OSA ISP. See View 7 for *PD*-OCT and View 8 for φ-OCT.

3.6. Case 5: PS-CASOCT of filtering bleb four-year after trabeculectomy

The patient was a 50-year-old Asian woman with a history of primary open-angle glaucoma in the right eye, and she was referred for ophthalmic examination to Kasumigaura Hospital, Tokyo Medical University. She underwent trabeculectomy in her right eye because of elevated IOP of 40 mm Hg, despite the administration of maximally tolerated pharmacological therapy.

Four years after the surgery, a non-functioning filtering bleb was observed on slit-lamp examination, as shown in Fig. 7(a). *PD*-OCT revealed the internal structure of the bleb. Several small fluid pools are observed as shown in Fig. 7(b) (the red arrows). The remnant of the fluid pool is also visible in the same image (green arrow). It is noteworthy that this region exhibited moderate birefringence, as observed on φ-OCT as shown in Fig. 7(c) (green arrow). This moderate birefringence may indicate abnormal fibrosis in this region.

The 3D interactive observation enables comprehensive and detailed observations of the *PD*-OCT and φ-OCT. These 3D datasets are available on-line. See View 7 for *PD*-OCT (35.9 MB) and View 8 for φ-OCT (35.9 MB).

A set of raw complex OCT volumes (1.0 GB) are also provided, which enables the readers to develop their own PS-OCT algorithm. For the details, see Appendix B.

4. Discussions and Conclusion

In patient 4, the area of the fluid pool was manually segmented by an experienced ophthalmologist by using a series of 2D cross-sectional tomographic images [16]. Although the segmented volume provided several clinically significant parameters, this process is time consuming and not applicable in the clinical setting. The development of an automated algorithm for the segmentation of the filtering bleb is an important future issue. The following engineering-related issues are expected during the automation process.

#99788 - $15.00 USD Received 5 Aug 2008; revised 22 Jan 2009; accepted 25 Jan 2009; published 2 Mar 2009

The signal strength of FD-OCT depends on the depth of the signal; i.e., the signal strength decays as a function of the distance from the zero-delay point of the OCT interferometer [10, 54]. This signal decay results in a systematic offset of the signal strength. Further, the signal strength and the image contrast of a tissue are strongly affected by the scattering properties of the superficial tissues. The development of a segmentation algorithm that is robust to these systematic and unsystematic signal perturbations is the next issue that should be addressed.

The contrast of the filtering bleb is related to the optical properties of the bleb tissues [55], and it varies from patient to patient. This difference in the contrast of the filtering bleb should be further investigated from a clinical perspective. Further knowledge of the OCT contrast of the filtering bleb will lead to improvements in the automatic segmentation algorithm.

The size and position of the incision or ablation site is important for trabeculotomy and laser iridotomy. For further analysis, it is crucial to automatically determine the shape of an incision site and the region of an ablation site.

Bullous keratopathy is an infrequent but serious complication of laser iridotomy [56, 57]. Alteration of the fluid-dynamic properties of aqueous humor after laser iridotomy is one of the suspected reasons for this complication [58]. The development of an accurate and automated segmentation algorithm will enable the creation of a complete 3D numerical model of the ablation site. This numerical model will in turn enable detailed analysis of the mechanical and fluid dynamic functions of the ablation site.

The φ-OCT images of subjects 3, 4, and 5 showed a variety of contrasts of the tissues around the filtering bleb. In contrast to φ-OCT, *PD*-OCT does not clearly differentiate among patients. Large variations in the contrast of φ-OCT may be related to the individual differences among subjects and variations in the interval between surgery and the performance of postoperative OCT. For example, it is known that fibrosis occasionally occurs in old filtering blebs. On the basis of the examination findings in the posterior eye segment, fibrosing tissue is selectively visualized by PS-OCT [48]. Such tissue properties are known to be related to the functions of the filtering bleb; hence, the assessment of tissue properties is crucial for the follow up of trabeculectomy. PS-CASOCT will enable routine noninvasive assessment of the filtering bleb.

Other than the evaluation of glaucoma surgeries, PS-CASOCT has more potential applications. Since PS-CASOCT visualizes trabecular meshwork with higher image-contrast than conventional CAS-OCT [49, 52], PS-CASOCT may be useful for the screening of angle closure glaucoma. Cornea consists of collagen and is known to be birefringent. This birefringent property may be useful for the evaluation of the abnormality of cornea, e.g. keratoconus [51].

In conclusion, 3 filtering blebs after trabeculectomy, and an incision site of trabeculotomy and an ablation site of laser iridotomy were examined by 3D-CASOCT and PS-CASOCT. The case series presented here is of clinical importance. The development of an automated quantitative image analysis technique will in the future provide results of greater clinical significance.

A. Appendix: Normal Anterior Chamber Angle

The anterior chamber angle (ACA) of a normal subject was examined using PS-CASOCT after obtaining written informed consent. The subject was a 48-year-old Asian man; no marked abnormality was present in his anterior eye. The details of the subject and the scanning protocol are presented in Tables 1 and 2 as subject 6. Although this result has already been presented in ref. [52], this appendix aims at providing a full 3D dataset of *PD*-OCT and φ-OCT as a reference standard of PS-CASOCT.

Figure 8 has been reprinted from ref. [52] and shows (a) *PD*-OCT, (b) φ-OCT, and (c) axis-orientation OCT images of the ACA. In the *PD*-OCT image (Fig. 8(a)), a trabecular meshwork (TM) appears as a diffuse hyper scattering region (indicated by an arrow). In contrast, the TM appears as a winding band in the φ-OCT. In the axis-orientation image, the variance of the

#99788 - $15.00 USD Received 5 Aug 2008; revised 22 Jan 2009; accepted 25 Jan 2009; published 2 Mar 2009

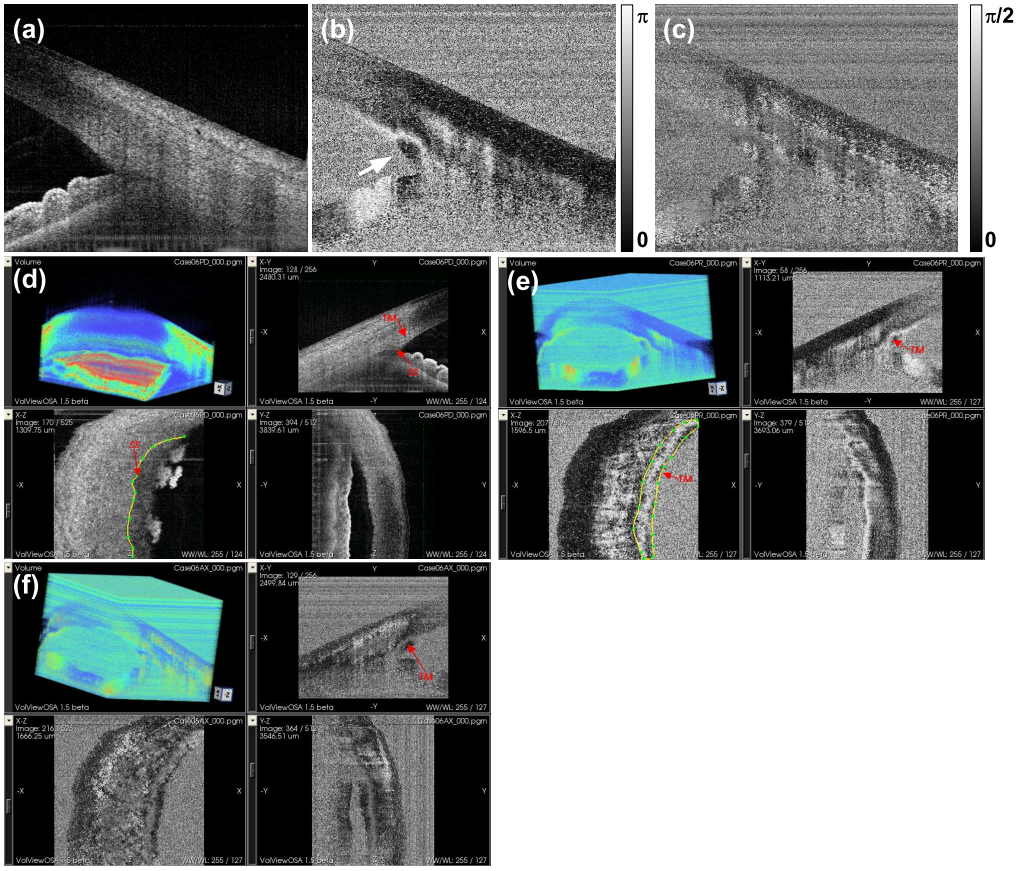

Fig. 8. Subject 6: The ACA of a normal subject. (a) *PD*-OCT, (b) φ-OCT, and (c) axis-orientation OCT. (d), (e), (f) Screen shots of 3D interactive observations of *PD*-OCT, φ-OCT and axis-orientation OCT by OSA ISP. The position of scleral spur (SS) and trabecular meshwork (TM) are indicated by red arrows and yellow curves. See View 9 for *PD*-OCT, View 10 for φ-OCT, and View 11 for axis-orientation OCT.

signal decreases at the TM because the TM shows strong birefringence, which results in a high signal-to-noise ratio. The 3D datasets are available on-line. See View 9 for *PD*-OCT (65.6 MB), View 10 for φ-OCT (65.6 MB), and View 11 for axis-orientation OCT (65.6 MB). A set of raw complex OCT volumes (1.9 GB) are also provided, which enables the readers to develop their own PS-OCT algorithm. For the details, see Appendix B.

B. Complex OCT Volumes

B.1. Data Format

One of the purposes of this paper is to provide a reference dataset of PS-OCT to developers and researchers who wish to develop their own PS-OCT algorithm. For this purpose, we provide raw complex OCT volumes of cases 3, 4, 5 and 6 as Interactive Science Publishing (ISP) datasets of Case0302 (case 3), Case0402 (case 4), Case0502 (case 5) and Case0603 (case 6). A set of OCT volumes of each case consists of 4 complex OCT volumes labeled as H0.csg, H1.csg, V0.csg, and V1.csg. Where H and V represent that the datasets were respectively acquired by horizontal and a vertical detection channels of PS-OCT, while 0 and 1 indicate whether this volume

#99788 - $15.00 USD Received 5 Aug 2008; revised 22 Jan 2009; accepted 25 Jan 2009; published 2 Mar 2009

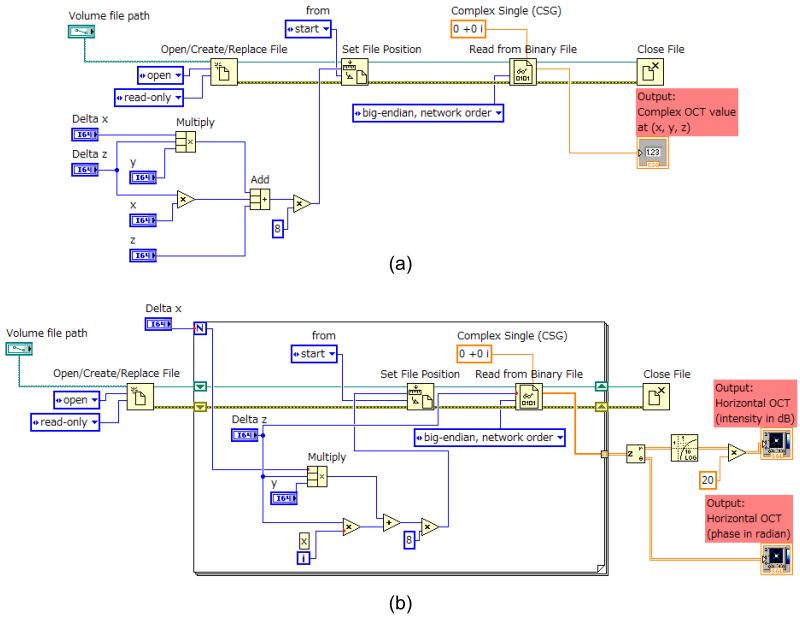

Fig. 9. Examples of LabVIEW programs. (a) A program to read a complex value at a single point in an OCT volume. (b) A program to read a single horizontal cross section from the volume.

is reconstructed from a non-intensity-modulated spectrum (0) or an intensity-modulated spectrum (1). For the details of these detection channels and the modulation, refer our previously published paper [52].

In these raw data volumes, numeric values are represented by a single precision complex (CSG, cmplx64) format of LabVIEW (National Instruments, TX), which is defined as the following code written in C. The data are stored with big-endian byte order.

```
typedef float float32;

typedef struct {
     float32 re, im;
} cmplx64;
```

The dimensions of the volumes are as summarized in Table 2. The data position of a point (x, y, z) in the volume file is calculated as

$$\text{Data position} = (\Delta x \times \Delta z \times y + \Delta z \times x + z) \times 8 \text{ bytes}, \tag{2}$$

where the data position is relative to the starting point of the file. Δx, Δy and Δz are the numbers of voxels along horizontal, vertical and depth directions, respectively, and x, y, and z are voxle indexes along the corresponding directions. The origin is set to nasal-superior-anterior corner of the OCT volume.

The examples of LabVIEW programs to read the OCT data are shown in Fig. 9. Figure 9(a) is a program which reads a complex value at a single point of an OCT volume, while Fig. 9(b) is for reading a single horizontal scan from the OCT volume.

#99788 - $15.00 USD Received 5 Aug 2008; revised 22 Jan 2009; accepted 25 Jan 2009; published 2 Mar 2009

B.2. Reconstruction of Jones Matrix

By using a set of the 4 complex OCT volumes, the Jones matrix of the sample is calculated as

$$\mathbf{J} = \begin{pmatrix} -H_0^* - H_1^*/\alpha & H_0^* - H_1^*/\alpha \\ -V_0^* - V_1^*/\alpha & V_0^* - V_1^*/\alpha \end{pmatrix}, \tag{3}$$

where H_0^*, H_1^*, V_0^* and V_1^* are complex conjugates of the complex OCT volumes of H0.csg, H1.csg, V0.csg and V1.csg. α is a constant which is defined as $J_1(2.405) = 0.5191098$, where J_1 is the first order Bessel function of the first kind. The detailes of the derivation of this equation is described in [52].

C. Appendix: Glaucoma Surgeries in Brief

C.1. Trabeculotomy

Trabeclulotomy is a glaucoma surgery which aims at creating a large opening between Schlemm's canal and the anterior eye chamber to reduce the drainage resistance of aqueous humor. In this surgery, 5/6 thickness of sclera close to the Schlemm's canal is, at first, temporarily peeled off. A thin metal bar, so called a trabeculotome, is inserted to the SC from this site, and the trabeculotome incises the Schlemm's canal and trabecular meshwork to the anterior eye chamber.

Since this surgery improve the drainage function of trabecular meshwork, mainly applied to corticosteroid glaucoma and capsular glaucoma, which are triggered by increased drainage resistance of trabecular meshwork.

C.2. Laser Iridotomy

Laser iridotomy is a glaucoma surgery which aims at reducing the difference of the pressures between anterior and posterior eye chambers, which is associated with the risk of pupillary block. Nd:YAG laser with a wavelength of 1064 nm is focus on an iris and ablates the iris tissue to create a bypass-channel between the anterior and posterior chambers.

Although the ablation hole with a diameter as small as 10 μm can reduce the pressure difference, a diameter of 200 μm is preferable to avoid the risk of future obturation.

C.3. Trabeculectomy

Trabeculectomy is a glaucoma surgery creating an artificial channel which drains the aqueous humor from the anterior eye chamber to the subconjunctival space. In this surgery, a surgeon incises a part of conjunctiva (a conjunctival flap), and a sclera in its partial-thickness (scleral flap). A knife or scissors approach to a trabecular meshwork from this flap region to the anterior chamber, and excise a part of the trabecular meshwork. The flaps are then tacked to their original positions. 0.04% mitomycin C liquid is frequently applied before the excision of the trabecular meshwork, to avoid the adhesion of flaps.

In the eyes treated by this surgery, the aqueous humor is drained to the sub-conjunctival-flap space through an artificial drainage channel created by the excision of the trabecular meshwork, and a fluid pool is created at the sub-confuntival space. The structure created by this surgery is referred to as a filtering bleb.

Acknowledgements

The technical support from Shuichi Makita, Atsushi Noguchi, and Arata Miyazawa of the University of Tsukuba are gratefully acknowledged. This study is partially supported by the Japan Society for the Promotion of Science (JSPS) through the Grant-in-aid for Scientific Research

#99788 - $15.00 USD Received 5 Aug 2008; revised 22 Jan 2009; accepted 25 Jan 2009; published 2 Mar 2009

15760026, the Japan Science and Technology Agency through the contract of the development program of advanced measurement systems, and a research grant from Tomey Corporation.

#99788 - $15.00 USD Received 5 Aug 2008; revised 22 Jan 2009; accepted 25 Jan 2009; published 2 Mar 2009